Research Article | Vol. 25, No. 4 | 20 Feb 2017 | OPTICS EXPRESS A134

Optics EXPRESS

Information content of bistatic lidar observations of aerosols from space

MIKHAIL D. ALEXANDROV[1,2,*] AND MICHAEL I. MISHCHENKO[2]

[1]*Columbia University, 2880 Broadway, New York, NY 10025, USA*
[2]*NASA Goddard Institute for Space Studies, 2880 Broadway, New York, NY 10025, USA*
[*]*mda14@columbia.edu*

Abstract: We present, for the first time, a quantitative retrieval error-propagation study for a bistatic high spectral resolution lidar (HSRL) system intended for detailed quasi-global monitoring of aerosol properties from space. Our results demonstrate that supplementing a conventional monostatic HSRL with an additional receiver flown in formation at a scattering angle close to 165° dramatically increases the information content of the measurements and allows for a sufficiently accurate characterization of tropospheric aerosols. We conclude that a bistatic HSRL system would far exceed the capabilities of currently flown or planned orbital instruments in monitoring global aerosol effects on the environment and on the Earth's climate. We also demonstrate how the commonly used *a priori* "regularization" methodology can artificially reduce the propagated uncertainties and can thereby be misleading as to the real retrieval capabilities of a measurement system.

OCIS codes: (010.3640) Lidar; (290.5820) Scattering measurements; (290.5850) Scattering, particles; (290.5855) Scattering, polarization.

References and links

1. D. Koch, T. C. Bond, D. Streets, N. Unger, and G. R. van der Werf, "Global impacts of aerosols from particular source regions and sectors," J. Geophys. Res. **112**, D02205 (2007).
2. N. Unger, D. T. Shindell, D. M. Koch, and D. G. Streets, "Air pollution radiative forcing from specific emissions sectors at 2030," J. Geophys. Res. **113**, D02306 (2008).
3. M. Chin, R. A. Kahn, and S. E. Schwartz, eds., *Atmospheric Aerosol Properties and Climate Impacts* (U.S. Climate Change Science Program, Washington, DC, 2009).
4. Z. Li, X. Zhao, R. Kahn, M. Mishchenko, L. Remer, K.-H. Lee, M. Wang, I. Laszlo, T. Nakajima, and H. Maring, "Uncertainties in satellite remote sensing of aerosols and impact on monitoring its long-term trend: a review and perspective," Ann. Geophys. **27**, 2755–2770 (2009).
5. N. G. Loeb and W. Su, "Direct aerosol radiative forcing uncertainty based on a radiative perturbation analysis," J. Clim. **23**, 5288–5293 (2010).
6. U. Lohmann and S. Ferrachat, "Impact of parametric uncertainties on the present-day climate and on the anthropogenic aerosol effect," Atmos. Chem. Phys. **10**, 11373–11383 (2010).
7. J. Hansen, M. Sato, P. Kharecha, and K. von Schuckmann, "Earth's energy imbalance and implications," Atmos. Chem. Phys. **11**, 13421–13449 (2011).
8. J. E. Penner, L. Xu, and M. Wang, "Satellite methods underestimate indirect climate forcing by aerosols," Proc. Natl. Acad. Sci. USA **108**, 13404–13408 (2011).
9. G. Myhre, B. H. Samset, M. Schulz, Y. Balkanski, S. Bauer, T. K. Berntsen, H. Bian, N. Bellouin, M. Chin, T. Diehl, R. C. Easter, J. Feichter, S. J. Ghan, D. Hauglustaine, T. Iversen, S. Kinne, A. Kirkevåg, J.-F. Lamarque, G. Lin, X. Liu, M. T. Lund, G. Luo, X. Ma, T. van Noije, J. E. Penner, P. J. Rasch, A. Ruiz, Ø. Seland, R. B. Skeie, P. Stier, T. Takemura, K. Tsigaridis, P. Wang, Z. Wang, L. Xu, H. Yu, F. Yu, J.-H. Yoon, K. Zhang, H. Zhang, and C. Zhou, "Radiative forcing of the direct aerosol effect from AeroCom Phase II simulations," Atmos. Chem. Phys. **13**, 1853–1877 (2013).
10. S. E. Schwartz, R. J. Charlson, and H. Rodhe, "Quantifying climate change – too rosy a picture?" Nat. Rep. Clim. Change **1**, 23–24 (2007).
11. National Research Council, *Earth Science and Applications from Space: National Imperatives for the Next Decade and Beyond* (The National Academies, 2007).
12. NASA Aerosol/Clouds/Ecosystems (ACE) mission, https://acemission.gsfc.nasa.gov.
13. E. Chemyakin, S. Burton, A. Kolgotin, D. Muller, C. Hostetler, and R. Ferrare, "Retrieval of aerosol parameters from multiwavelength lidar: investigation of the underlying inverse mathematical problem," Appl. Opt. **55**, 2188–2202 (2016).

#282561 https://doi.org/10.1364/OE.25.00A134
Journal © 2017 Received 9 Dec 2016; revised 19 Jan 2017; accepted 20 Jan 2017; published 3 Feb 2017

Optics EXPRESS

14. S. P. Burton, E. Chemyakin, X. Liu, K. Knobelspiesse, S. Stamnes, P. Sawamura, R. H. Moore, C. A. Hostetler, and R. A. Ferrare, "Information content and sensitivity of the $3\beta + 2\alpha$ lidar measurement system for aerosol microphysical retrievals," Atmos. Meas. Tech. **9**, 5555–5574 (2016).
15. K. Knobelspiesse, B. Cairns, M. Ottaviani, R. Ferrare, J. Hair, C. Hostetler, M. Obland, R. Rogers, J. Redemann, Y. Shinozuka, A. Clarke, S. Freitag, S. Howell, V. Kapustin, and C. McNaughton, "Combined retrievals of boreal forest fire aerosol properties with a polarimeter and lidar," Atmos. Chem. Phys. **11**, 7045–7067 (2011).
16. M. I. Mishchenko, M. D. Alexandrov, B. Cairns, and L. D. Travis, "Multistatic aerosol-cloud lidar in space: a theoretical perspective," J. Quant. Spectrosc. Radiat. Transfer **184**, 180–192 (2016).
17. P. J. Rogers and P. Eccles, "The bistatic radar equation for randomly distributed targets," Proc. IEEE **59**, 1019–1021 (1971).
18. J. A. Reagan, D. M. Byrne, and B. M. Herman, "Bistatic LIDAR: a tool for characterizing atmospheric particulates: Part I – The remote sensing problem," IEEE Trans. Geosci. Remote Sens. **20**, 229–235 (1982).
19. J. A. Reagan, D. M. Byrne, and B. M. Herman, "Bistatic LIDAR: a tool for characterizing atmospheric particulates: Part II – The inverse problem," IEEE Trans. Geosci. Remote Sens. **20**, 236–243 (1982).
20. C. D. Rodgers, *Inverse Methods for Atmospheric Sounding: Theory and Practice* (World Scientific, 2000).
21. S. T. Shipley, D. H. Tracy, E. W. Eloranta, J. T. Trauger, J. T. Sroga, F. L. Roesler, and W. J. A., "A High Spectral Resolution Lidar to measure optical scattering properties of atmospheric aersols. Part I: Intrumentation and theory," Appl. Opt. **23**, 3716–3724 (1983).
22. E. E. Eloranta, "High spectral resolution lidar," in *Lidar: Range-Resolved Optical Remote Sensing of the Atmosphere*, C. Weitkamp, ed. (Springer, 2005), pp. 143–163.
23. J. W. Hair, C. A. Hostetler, A. L. Cook, D. B. Harper, R. A. Ferrare, T. L. Mack, W. Welch, L. R. Izquierdo, and F. E. Hovis, "Airborne High Spectral Resolution Lidar for profiling aerosol optical properties," Appl. Opt. **47**, 6734–6752 (2008).
24. J. E. Hansen and L. D. Travis, "Light scattering in planetary atmospheres," Space. Sci. Rev. **16**, 527–610 (1974).
25. H. C. van de Hulst, *Light Scattering by Small Particles* (Wiley, 1957).
26. M. I. Mishchenko, L. D. Travis, and A. A. Lacis, *Scattering, Absorption, and Emission of Light by Small Particles* (Cambridge University, 2002).
27. J. W. Hovenier, C. van der Mee, and H. Domke, *Transfer of Polarized Light in Planetary Atmospheres – Basic Concepts and Practical Methods* (Kluwer, 2004).
28. M. I. Mishchenko, *Electromagnetic Scattering by Particles and Particle Groups: an Introduction* (Cambridge University, 2014).
29. I. Veselovskii, A. Kolgotin, V. Griaznov, D. Müller, U. Wandinger, and D. N. Whiteman, "Inversion with regularization for the retrieval of tropospheric aerosol parameters from multi-wavelength lidar sounding," Appl. Opt. **41**, 3685–3699 (2002).
30. W. Su, G. L. Schuster, N. G. Loeb, R. R. Rogers, R. A. Ferrare, C. A. Hostetler, J. W. Hair, and M. D. Obland, "Aerosol and cloud interaction observed from high spectral resolution lidar data," J. Geophys. Res. **113**, D24202 (2008).
31. I. Veselovskii, O. Dubovik, A. Kolgotin, M. Korenskiy, D. N. Whiteman, K. Allakhverdiev, and F. Huseyinoglu, "Linear estimation of particle bulk parameters from multi-wavelength lidar measurements," Atmos. Meas. Tech. **5**, 1135–1145 (2012).
32. D. Müller, C. A. Hostetler, R. A. Ferrare, S. P. Burton, E. Chemyakin, A. Kolgotin, J. W. Hair, A. L. Cook, D. B. Harper, R. R. Rogers, R. W. Hare, C. S. Cleckner, M. D. Obland, J. Tomlinson, L. K. Berg, and B. Schmid, "Airborne Multiwavelength High Spectral Resolution Lidar (HSRL-2) observations during TCAP 2012: vertical profiles of optical and microphysical properties of a smoke/urban haze plume over the northeastern coast of the US," Atmos. Meas. Tech. **7**, 3487–3496 (2014).
33. M. I. Mishchenko, B. Cairns, J. E. Hansen, L. D. Travis, R. Burg, Y. J. Kaufman, J. V. Martins, and E. P. Shettle, "Monitoring of aerosol forcing of climate from space: analysis of measurement requirements," J. Quant. Spectrosc. Radiat. Transfer **88**, 149–161 (2004).
34. D. T. L. Alexander, P. A. Crozier, and J. R. Anderson, "Brown carbon spheres in east asian outflow and their optical properties," Science **321**, 833–835 (2008).
35. D. M. Winker, M. A. Vaughan, A. Omar, Y. Hu, K. A. Powell, Z. Liu, W. H. Hunt, and S. A. Young, "Overview of the CALIPSO mission and CALIOP data processing algorithms," J. Atmos. Oceanic. Technol. **26**, 2310–2323 (2009).
36. G. L. Stephens, D. G. Vane, S. Tanelli, E. Im, S. Durden, M. Rokey, D. Reinke, P. Partain, G. G. Mace, R. Austin, T. L'Ecuyer, J. Haynes, M. Lebsock, K. Suzuki, D. Waliser, D. Wu, J. Kay, A. Gettleman, Z. Wang, and R. Marchand, "CloudSat mission: performance and early science after the first year of operation," J. Geophys. Res. **113**, D00A18 (2008).
37. G. Krieger, A. Moreira, H. Fiedler, I. Hajnsek, M. Werner, M. Younis, and M. Zink, "TanDEM-X: a satellite formation for high-resolution SAR interferometry," IEEE Trans. Geosci. Remote. Sens. **45**, 3317–3341 (2007).

Optics EXPRESS

1. Introduction

Atmospheric aerosols through their direct and indirect radiative effects cause significant uncertainties in our understanding and assessment of global climate change [1–9]. These uncertainties are, in fact, so large that they preclude definitive climate model evaluation by comparison with the observed global temperature change and must be reduced by at least a factor of three [10]. Achieving this goal requires a comprehensive global aerosol-monitoring program with three major science objectives [3]: the determination of the global distribution of aerosol and cloud properties; the evaluation of the direct aerosol effect on the Earth's radiation budget; and the quantification of the effects of aerosols on clouds and precipitation.

Toward meeting these objectives, National Research Council's 2007 Earth Decadal Survey [11] recommended a NASA Aerosol/Clouds/Ecosystems (ACE) satellite mission [12]. This mission is intended to provide a quasi-global 3D dataset of aerosol properties suitable for constraining aerosol transport models, thereby facilitating accurate aerosol forcing estimates and global climate predictions. The ACE mission is planned to include a multi-wavelength high spectral resolution lidar (HSRL) whose data are expected to yield the quasi-global distribution of vertically resolved aerosol microphysical characteristics.

Current retrieval algorithms for the HSRL (heavily relying on various regularization procedures) use the combination of backscattering coefficients in three spectral channels and extinction coefficients in two channels, commonly referred to as "$3\beta + 2\alpha$". The results of recent studies [13, 14] suggest that without strong *a priori* constraints the "$3\beta + 2\alpha$" dataset is underdetermined with respect to the full suite of requisite microphysical aerosol parameters and that additional coincident measurements are required in order to facilitate accurate retrievals. In some cases such supplementary data could be provided by, e.g., a polarimeter [15].

An alternative methodology was outlined in a recent perspective [16] and contemplates flying one or more secondary receivers of scattered laser light on separate satellites in formation with the main platform carrying the HSRL. Such receivers would measure the laser signals scattered by aerosol particles at different angles in addition to the exact backscattering direction, thereby providing supplementary information that can help better constrain the retrievals.

Note that the idea of a bi/multistatic lidar measurement system is not new. The general geometric layout of a bistatic radar configuration and the corresponding equation were described in detail by Rogers and Eccles in 1971 [17] and later adapted (in a simplified form) to lidar remote sensing by Reagan et al. [18, 19]. While several ground-based bi- and multistatic lidar systems have been built since the 1980s, airborne instruments are still in the concept-development phase (see [16] for further references).

Although the qualitative discussion in [16] is strongly indicative of a great aerosol-characterization potential of a bistatic HSRL configuration, it needs to be supplemented by an explicit quantitative demonstration. This paper is a natural extension of [16] in that it presents the results of a numerical sensitivity analysis of the retrieval accuracy of a bistatic HSRL system. We use a linearized error-propagation model based on [20] to parallel the recent evaluation of the conventional "$3\beta + 2\alpha$" technique based on a monostatic HSRL [14]. In this way we provide the first ever quantitative assessment of the great improvement rendered by the addition of a secondary detector. An important byproduct of our study is the demonstration of a potentially misleading effect of invoking *a priori* constraints in assessing the likely accuracy of a retrieval methodology.

2. Bistatic lidar system

In this study we follow the conventions and notation of [16] which we will briefly outline here. There and in this paper the term "bistatic lidar system" refers to a combination of the conventional backscattering lidar (with both the laser beam and the receiver pointed at nadir)

Optics EXPRESS

and one additional receiver with the outward optical axis constituting an angle $180° - \Theta$ with the transmitted beam direction. Here Θ is the scattering angle, i.e., the angle between the incidence (nadir in our case) and scattering directions. The Stokes parameters of both the transmitted and the scattered laser light are defined with respect to the scattering plane, which coincides in this case with the meridional plane of the scattered beam. The Stokes column vectors of the scattered lidar returns at the two receivers and that of the transmitted (incident) laser beam are, respectively,

$$\mathbf{I}_{\mathrm{a}}^{\mathrm{sca}}(\Theta) = \begin{pmatrix} I_{\mathrm{a}}^{\mathrm{sca}}(\Theta) \\ Q_{\mathrm{a}}^{\mathrm{sca}}(\Theta) \\ U_{\mathrm{a}}^{\mathrm{sca}}(\Theta) \\ V_{\mathrm{a}}^{\mathrm{sca}}(\Theta) \end{pmatrix}, \quad \mathbf{I}_{\mathrm{b}}^{\mathrm{sca}} = \begin{pmatrix} I_{\mathrm{b}}^{\mathrm{sca}} \\ Q_{\mathrm{b}}^{\mathrm{sca}} \\ U_{\mathrm{b}}^{\mathrm{sca}} \\ V_{\mathrm{b}}^{\mathrm{sca}} \end{pmatrix}, \quad \text{and} \quad \mathbf{I}^{\mathrm{inc}} = \begin{pmatrix} I^{\mathrm{inc}} \\ Q^{\mathrm{inc}} \\ U^{\mathrm{inc}} \\ V^{\mathrm{inc}} \end{pmatrix}, \tag{1}$$

where the subscripts "a" and "b" stand for "additional" and "backscatter", respectively. These vectors satisfy the system of bistatic lidar equations:

$$\mathbf{I}_{\mathrm{a}}^{\mathrm{sca}}(\Theta) = T_1\, T_2(\Theta)\, \mathbf{F}^{\mathrm{V}}(\Theta)\, \mathbf{I}^{\mathrm{inc}}, \tag{2}$$

$$\mathbf{I}_{\mathrm{b}}^{\mathrm{sca}} = T_1^2\, \mathbf{F}^{\mathrm{V}}(180°)\, \mathbf{I}^{\mathrm{inc}}. \tag{3}$$

Here we assume that the geometric factor depending on specific transmitter–receiver configuration is always known and is omitted for simplicity. In Eqs. (2) and (3), T_1 is the scalar exponential attenuation factor corresponding to the vertical light path from the laser to the scattering volume, while $T_2(\Theta)$ is the scalar exponential attenuation factor corresponding to the slanted light path from the scattering volume to the receiver. $\mathbf{F}^{\mathrm{V}}(\Theta)$ is the local scattering matrix per unit volume of the atmosphere. In general, it has a particulate (aerosol in our case) and a Rayleigh component:

$$\mathbf{F}^{\mathrm{V}}(\Theta) = \frac{k_{\mathrm{sca}}^{\mathrm{p}}}{4\pi}\, \mathbf{F}^{\mathrm{p}}(\Theta) + \frac{k_{\mathrm{sca}}^{\mathrm{R}}}{4\pi}\, \mathbf{F}^{\mathrm{R}}(\Theta), \tag{4}$$

where $\mathbf{F}^{\mathrm{p}}(\Theta)$ and $\mathbf{F}^{\mathrm{R}}(\Theta)$ are, respectively, the particulate and Rayleigh 4×4 normalized scattering matrices, while $k_{\mathrm{sca}}^{\mathrm{p}}$ and $k_{\mathrm{sca}}^{\mathrm{R}}$ are the corresponding particulate and Rayleigh scattering coefficients.

3. HSRL

The HSRL technique [21–23] uses spectral broadening of the lidar return from the gaseous atmosphere, which allows for the separation between the gaseous and particulate returns:

$$\mathbf{I}_{\mathrm{a}}^{\mathrm{sca}}(\Theta) = \mathbf{I}_{\mathrm{a}}^{\mathrm{sca,p}}(\Theta) + \mathbf{I}_{\mathrm{a}}^{\mathrm{sca,R}}(\Theta), \quad \mathbf{I}_{\mathrm{b}}^{\mathrm{sca}} = \mathbf{I}_{\mathrm{b}}^{\mathrm{sca,p}} + \mathbf{I}_{\mathrm{b}}^{\mathrm{sca,R}}, \tag{5}$$

where

$$\mathbf{I}_{\mathrm{a}}^{\mathrm{sca,p}}(\Theta) = T_1\, T_2(\Theta)\, \frac{k_{\mathrm{sca}}^{\mathrm{p}}}{4\pi}\, \mathbf{F}^{\mathrm{p}}(\Theta)\, \mathbf{I}^{\mathrm{inc}}, \quad \mathbf{I}_{\mathrm{b}}^{\mathrm{sca,p}} = T_1^2\, \frac{k_{\mathrm{sca}}^{\mathrm{p}}}{4\pi}\, \mathbf{F}^{\mathrm{p}}(180°)\, \mathbf{I}^{\mathrm{inc}}, \tag{6}$$

$$\mathbf{I}_{\mathrm{a}}^{\mathrm{sca,R}}(\Theta) = T_1\, T_2(\Theta)\, \frac{k_{\mathrm{sca}}^{\mathrm{R}}}{4\pi}\, \mathbf{F}^{\mathrm{R}}(\Theta)\, \mathbf{I}^{\mathrm{inc}}, \quad \mathbf{I}_{\mathrm{b}}^{\mathrm{sca,R}} = T_1^2\, \frac{k_{\mathrm{sca}}^{\mathrm{R}}}{4\pi}\, \mathbf{F}^{\mathrm{R}}(180°)\, \mathbf{I}^{\mathrm{inc}}. \tag{7}$$

Given that the vertical profile of $k_{\mathrm{sca}}^{\mathrm{R}}$ is usually assumed to be known, and the Rayleigh scattering matrix has a simple analytical form [24], Eqs. (7) yield the products $T_1 T_2(\Theta)$ and T_1^2. These products are then used in Eqs. (6) to derive the combinations $k_{\mathrm{sca}}^{\mathrm{p}}\, \mathbf{F}^{\mathrm{p}}\, \mathbf{I}^{\mathrm{inc}}$. The attenuation factor T_1 is also used for the retrieval of the extinction coefficient $k_{\mathrm{ext}}^{\mathrm{p}}$.

Optics EXPRESS

In this study all aerosol particles are assumed to be spherically symmetric. For such particles the normalized scattering matrix has a particularly simple form with only four independent elements [25–28]:

$$\mathbf{F}^{\mathrm{p}}(\Theta) = \begin{pmatrix} F_{11}^{\mathrm{p}}(\Theta) & F_{12}^{\mathrm{p}}(\Theta) & 0 & 0 \\ F_{12}^{\mathrm{p}}(\Theta) & F_{11}^{\mathrm{p}}(\Theta) & 0 & 0 \\ 0 & 0 & F_{33}^{\mathrm{p}}(\Theta) & F_{34}^{\mathrm{p}}(\Theta) \\ 0 & 0 & -F_{34}^{\mathrm{p}}(\Theta) & F_{33}^{\mathrm{p}}(\Theta) \end{pmatrix}. \tag{8}$$

Note that in the backscattering direction,

$$F_{12}^{\mathrm{p}}(180^\circ) = F_{34}^{\mathrm{p}}(180^\circ) = 0 \quad \text{and} \quad F_{33}^{\mathrm{p}}(180^\circ) = -F_{11}^{\mathrm{p}}(180^\circ), \tag{9}$$

so that only a single matrix element survives:

$$\mathbf{F}^{\mathrm{p}}(180^\circ) = \begin{pmatrix} 1 & 0 & 0 & 0 \\ 0 & 1 & 0 & 0 \\ 0 & 0 & -1 & 0 \\ 0 & 0 & 0 & -1 \end{pmatrix} F_{11}^{\mathrm{p}}(180^\circ). \tag{10}$$

The structure of the scattering matrix (8) allows for a direct measurement of its elements with an appropriate polarization of the transmitted laser beam [16, 24]. We assume the transmitted beam to be fully linearly polarized at 45° relative to the scattering plane. In this case the only non-zero components of the incident Stokes vector are I^{inc} and $U^{\mathrm{inc}} = I^{\mathrm{inc}}$:

$$\mathbf{I}^{\mathrm{inc}} = \begin{pmatrix} 1 \\ 0 \\ 1 \\ 0 \end{pmatrix} I^{\mathrm{inc}}. \tag{11}$$

Hence

$$k_{\mathrm{sca}}^{\mathrm{p}}\, \mathbf{F}^{\mathrm{p}}(\Theta)\, \mathbf{I}^{\mathrm{inc}} = I^{\mathrm{inc}}\, k_{\mathrm{sca}}^{\mathrm{p}} \begin{pmatrix} F_{11}^{\mathrm{p}}(\Theta) \\ F_{12}^{\mathrm{p}}(\Theta) \\ F_{33}^{\mathrm{p}}(\Theta) \\ -F_{34}^{\mathrm{p}}(\Theta) \end{pmatrix} \tag{12}$$

and

$$k_{\mathrm{sca}}^{\mathrm{p}}\, \mathbf{F}^{\mathrm{p}}(180^\circ)\, \mathbf{I}^{\mathrm{inc}} = I^{\mathrm{inc}}\, k_{\mathrm{sca}}^{\mathrm{p}}\, F_{11}^{\mathrm{p}}(180^\circ) \begin{pmatrix} 1 \\ 0 \\ -1 \\ 0 \end{pmatrix}. \tag{13}$$

Assuming that the intensity of the incident laser beam is known, we obtain from a single-wavelength HSRL measurement the following quantities implicitly characterizing the properties of the atmospheric particles:

$$\alpha = k_{\mathrm{ext}}^{\mathrm{p}}, \tag{14}$$

$$\beta = k_{\mathrm{sca}}^{\mathrm{p}}\, F_{11}^{\mathrm{p}}(180^\circ), \tag{15}$$

$$\gamma_{11} = k_{\mathrm{sca}}^{\mathrm{p}}\, F_{11}^{\mathrm{p}}(\Theta), \tag{16}$$

$$\gamma_{12} = k_{\mathrm{sca}}^{\mathrm{p}}\, F_{12}^{\mathrm{p}}(\Theta), \tag{17}$$

$$\gamma_{33} = k_{\mathrm{sca}}^{\mathrm{p}}\, F_{33}^{\mathrm{p}}(\Theta), \tag{18}$$

$$\gamma_{34} = k_{\mathrm{sca}}^{\mathrm{p}}\, F_{34}^{\mathrm{p}}(\Theta), \tag{19}$$

Optics EXPRESS

Table 1. Expected variability ranges of the state vector elements

	r_{eff}, μm	v_{eff}	m_r	m_i	N_{c}, cm^{-3}
min	0.02	0.1	1.33	0.0	1
max	2	0.5	1.90	0.3	40000
1/2 range	1	0.2	0.29	0.15	20000

where α and β are, respectively, the extinction and backscattering coefficients derived from the traditional monostatic HSRL measurement, while γ_{ij} are supplementary parameters obtained using the additional receiver in the bistatic lidar system.

Typically HSRL operates at three wavelengths: 355, 532, and 1064 nm. In the case of the traditional monostatic lidar the particulate parameters are retrieved from the measurement of the backscattering coefficients at all three wavelengths and the extinction coefficients at 355 and 532 nm using the "$3\beta+2\alpha$" technique [13,29–32]. With only five units of data per scattering volume, this technique has been demonstrated [13, 14] to be incapable of solving the ill-posed inverse particle-characterization problem involving many more unknown parameters than five [33].

4. Propagated retrieval uncertainties

In a recent paper [14] the information content of the "$3\beta + 2\alpha$" measurements was analyzed assuming a 5-parameter aerosol model and using the error-propagation framework described by Rodgers [20]. In this study we will evaluate the information content of bistatic lidar system measurements of Eqs. (14)–(19) made at the three HSRL wavelengths (i.e., with no $k_{\text{ext}}^{\text{p}}$ retrievals in the 1064-nm channel). Such a bistatic measurement set can be called "$12\gamma+3\beta+2\alpha$", by analogy with the monostatic "$3\beta + 2\alpha$" set whose information content will be also evaluated for comparison. Thus, the measurement vector of the bistatic lidar system has 17 elements.

We will use a simple aerosol model similar to that of [14]. In this model we assume that the aerosol particles are homogeneous spheres, and that the aerosol population is monomodal and characterized by a gamma size distribution. This size distribution is fully parameterized by the effective radius (r_{eff}) and variance (v_{eff}) [24]. Other parameters of the aerosol model are the real (m_r) and imaginary (m_i) parts of the refractive index (both assumed to be wavelength independent), as well as the aerosol number concentration N_{c}. Thus, the aerosol state vector has five elements:

$$\mathbf{X} = \begin{pmatrix} r_{\text{eff}} \\ v_{\text{eff}} \\ m_r \\ m_i \\ N_{\text{c}} \end{pmatrix}. \tag{20}$$

The expected variability ranges of the state vector elements are summarized in Table 1.

In forward modeling, the Lorenz–Mie theory [25, 26] is used to compute the elements of the particle normalized scattering matrix and the extinction and scattering cross sections ($C_{\text{ext}}^{\text{p}}$ and $C_{\text{sca}}^{\text{p}}$, respectively). The corresponding coefficients are given by

$$k_{\text{ext}}^{\text{p}} = C_{\text{ext}}^{\text{p}}\, N_{\text{c}} \quad \text{and} \quad k_{\text{sca}}^{\text{p}} = C_{\text{sca}}^{\text{p}}\, N_{\text{c}}. \tag{21}$$

This computational procedure resulting in the 17-element measurement vector $\mathbf{Y}$ (Eqs. (14)–

Optics EXPRESS

(19)) can be expressed as some function **F** applied to the state vector **X** defined by Eq. (20):

$$\mathbf{Y} = \mathbf{F}(\mathbf{X}) + \boldsymbol{\varepsilon}, \tag{22}$$

where $\boldsymbol{\varepsilon}$ represents the measurement noise. This equation can be linearized in the neighborhood of some state vector $\mathbf{X}^0$:

$$\mathbf{Y} = \mathbf{F}(\mathbf{X}^0) + \mathbf{J}\,(\mathbf{X} - \mathbf{X}^0) + \boldsymbol{\varepsilon}, \tag{23}$$

where **J** is the Jacobian matrix of the function **F** at $\mathbf{X}^0$ having matrix elements of the form

$$J_{ij} = \left.\frac{\partial F_i(\mathbf{X})}{\partial X_j}\right|_{\mathbf{X}^0}. \tag{24}$$

The measurement-error vector $\boldsymbol{\varepsilon}$ is assumed to be a random vector obeying a multi-dimensional normal probability density function (PDF) characterized by the error covariance matrix $\mathbf{S}_{\boldsymbol{\varepsilon}}$ [20]. Following [14] we assume that all measurements are independent, hence the error covariance matrix is diagonal with the non-zero elements equal to squared standard deviations of the measurement vector elements. The measurement accuracy for the extinction coefficient α is assumed to be 20%, while that for the backscattering coefficient β is assumed to be 5% [14]. We assume the measurements of the bistatic coefficients γ to have the same absolute accuracy as the backscattering coefficients (5% of β).

The measurement uncertainties can be propagated into those of the retrieved state vector [20]. The following relationship exists between the retrieval error covariance matrix **S** and its measurement counterpart $\mathbf{S}_{\boldsymbol{\varepsilon}}$:

$$\mathbf{S}^{-1} = \mathbf{J}^T\,\mathbf{S}_{\boldsymbol{\varepsilon}}^{-1}\,\mathbf{J}, \tag{25}$$

where "*T*" stands for "transposed". The diagonal elements of the error covariance matrix **S** provide standard deviations of the corresponding state vector components.

5. Summa contra Rodgers

Note that there is a difference between Eq. (25) and its counterpart in Rodgers [20]. The latter includes an additional term corresponding to the *a priori* expectation of the retrieval results:

$$\mathbf{S}^{-1} = \mathbf{J}^T\,\mathbf{S}_{\boldsymbol{\varepsilon}}^{-1}\,\mathbf{J} + \mathbf{S}_{\mathrm{a}}^{-1}. \tag{26}$$

In that approach the subjective "prior knowledge" of the retrieval outcome is treated as an independent retrieval (which it is not), thereby being on equal footing with the real ones. The assumption that the PDF of the *a priori* state vector is Gaussian (with some pre-assumed mean value and covariance matrix $\mathbf{S}_{\mathrm{a}}$) is characterized by Rodgers himself as "less realistic, but convenient". The Rodger's Bayesian approach can be viewed as a variant of data assimilation rather than a retrieval concept. Indeed, the *a priori* PDF can be treated as a (non-dynamical) model which is adjusted by assimilating measurement results. Although this is a legitimate concept, the mean of the adjusted PDF cannot be called "retrieval" and its standard deviation – "the accuracy" of this "retrieval". Otherwise, such approach results in a subjective distortion of the retrieval results by forcing the retrieved state vector to be closer to the pre-assumed value. It also reduces the retrieval uncertainty, thereby making the retrieval look better than it actually is. We agree that an existing common knowledge about the range of the state vector variability can be used in the evaluation of the information content of the measurement (we included Table 1 for this very reason). However, prior knowledge under no circumstances should play an active role, influencing retrieval results and estimates of their accuracy. Unfortunately, the popularity

Optics EXPRESS

Table 2. Measurement accuracy requirements for quantification of aerosol effects on climate [14, 33]

Accuracy	r_{eff}, μm	v_{eff}	m_r	ϖ_0	N_c, cm^{-3}
Absolute	0.1	0.3	0.02	0.03	–
Relative	10%	50%	–	–	100%

of the Rodger's book makes it somewhat problematic to convince the scientific community to have a more critical look at its treatment of *a priori* information. In this study we will use Eq. (25) to estimate the retrieval uncertainties, while Eq. (26) will serve for the demonstration of the impact of the "prior knowledge" use according to [20]. In the latter case we will follow [14] by assuming the *a priori* state variables to be uncorrelated and having standard deviations equal to one half of their respective variability ranges (indicated in the bottom row of Table 1).

6. Degrees of freedom in the measurements

Common knowledge of the state vector variability can play an important role in the evaluation of "usefulness" of the measurement (given its nature and accuracy) by estimating the amount of new information that it provides compared to what is already known. In this regard, we find instructive the number of degrees of freedom (DOF) described in [20] as a metric quantifying the information content of a measurement. The DOF is defined as the number of independent units of information in the measurement determined with the accuracy better than the *a priori* constraints. For an ideal measurement system the DOF would be equal to the number of state parameters (five in our study). There are two methods for the DOF computation described in [20]. One defines the DOF as the number of singular values (SVs) of the matrix

$$\tilde{\mathbf{J}} = \mathbf{S}_{\boldsymbol{\varepsilon}}^{-\frac{1}{2}}\,\mathbf{J}\,\mathbf{S}_{\text{a}}^{\frac{1}{2}} \tag{27}$$

that are greater than "about unity". This number is equal to the number of eigenvalues of $\tilde{\mathbf{J}}^T\tilde{\mathbf{J}}$ having the same property. Note that in our model both $\mathbf{S}_{\boldsymbol{\varepsilon}}$ and $\mathbf{S}_{\text{a}}$ are diagonal, so the computation of their square roots is straightforward. This method is independent of the Bayesian approach and effectively provides a measure of sensitivity of the measurement variation (normalized by the error) to the variation of the state vector (normalized by the variability range). Another DOF estimate is based on the Bayesian approach in the linear Gaussian case and has the following quantitative expression:

$$d_{\text{s}} = \text{tr}\left[\left(\mathbf{J}^T\,\mathbf{S}_{\boldsymbol{\varepsilon}}^{-1}\,\mathbf{J} + \mathbf{S}_{\text{a}}^{-1}\right)^{-1}\mathbf{J}^T\,\mathbf{S}_{\boldsymbol{\varepsilon}}^{-1}\,\mathbf{J}\right], \tag{28}$$

where "tr" stands for "trace". Note that unlike the DOF based on the number of singular values, d_{s} is not necessarily an integer.

7. Case studies

In this section we present the results of four case studies associated with specific choices of the state vector $\mathbf{X}^0$. In each case the Jacobian matrices were computed by differentiating the output of the Lorentz–Mie FORTRAN program [26]. In order to derive the matrix element J_{ij}, the elements of the measurement vector component Y_i were first computed for the three

Optics EXPRESS

state vectors having the same elements as $\mathbf{X}_0$, except for the j's element, which was varied within 5%: $0.95X_j^0$, X_j^0, and $1.05X_j^0$. These three data points were then used for the derivation of the coefficients of a unique quadratic function that connects them. As the final step, the derivative at X_j^0 was evaluated analytically using these coefficients. This method is more robust then that based on finite differences, since it accounts for the local curvature of the function that is being differentiated. The choice of a 5% step is not crucial; tests with different values revealed only insignificant differences. The measurement error covariance matrix $\mathbf{S}_\varepsilon$ was determined as described in Section 4 (20% for α, 5% for β and γ). In each case separate computations were performed for the "$12\gamma + 3\beta + 2\alpha$" and "$3\beta + 2\alpha$" configurations.

The retrieval accuracy thresholds for the reliable quantification of the aerosol effects on climate are summarized in Table 2 (if both absolute and relative uncertainties are present, the greater of them is assumed). These numbers were initially reported in [33] and later adopted (with some modifications) by the NASA ACE Project (cf. [14]).

The four aerosol cases were selected to be similar to those chosen in the previous "$3\beta + 2\alpha$" sensitivity study [14]. They include weakly absorbing fine 0.17-μm particles (Case 1) characteristic of urban emissions; larger 0.5-μm particles (Case 2); and large coarse-mode aerosol with $r_{\text{eff}} = 1.6$ μm representing sea spray aerosols (Case 3). In addition, we included Case 4 of highly absorbing brown-carbon spheres [34] with $r_{\text{eff}} = 0.12$ μm and $m_i = 0.27$.

One of the goals of this study is to find the optimal scattering angle Θ for the additional HSRL receiver. Figures 1–4 quantify the dependence of the propagated uncertainties on Θ over the most interesting range from 160°–180° where the elements of the scattering matrix exhibit the strongest variability with (and hence the strongest sensitivity to) particle size and refractive index [16]. We have not considered smaller scattering angles since they seem to be less practical from the point of view of satellite formation flying, and also because cirrus clouds may stronger affect the measurements at such angles (see the discussion in [16]). The state parameters and their propagated standard deviations for all four cases are summarized in Table 3. While there $\Theta = 165°$ has been chosen as the reference scattering angle, it can be seen from Figs. 1–4 that any angle between 160° and 170° can be equally satisfactory. Studies involving more complex aerosol models (such as bimodal) may help narrow this range down.

Figures 1–4 show the ratios of the propagated standard deviations to the actual values of the corresponding state vector elements. The relative standard deviation values for the "$3\beta + 2\alpha$" configuration are depicted by the arrows on the right-hand vertical axes. Note that they are always larger than their "$12\gamma+3\beta+2\alpha$" counterparts corresponding to $\Theta = 180°$ because the latter configuration includes redundant yet independent backscatter measurements made by the second receiver. The top panels of each figure present the actual propagated uncertainties computed using Eq. (25), while the respective bottom panels demonstrate the artificial "improvement" of the measurement accuracy if Rodger's "regularization" (26) is applied. Based on these plots, we selected $\Theta = 165°$ as a good candidate for the additional-receiver scattering angle. Note also that the uncertainties of the "$12\gamma + 3\beta + 2\alpha$" retrievals using this angle are so small that they are hardly improved by the *a priori* regularization procedure (except for m_i in Case 4).

The state parameters and their propagated standard deviations for all four cases are summarized in Table 3. The uncertainties are presented for the "$3\beta + 2\alpha$" and "$12\gamma + 3\beta + 2\alpha$" configurations, the latter corresponding to $\Theta = 165°$. We also show for comparison the "$3\beta + 2\alpha$" results obtained using Rodger's *a priori* regularization. These values are crossed out by red lines in Table 3 to emphasize that they are not methodologically admissible. The arrow superscripts indicate that the state parameter values within one standard deviation from the mean violate the upper (↑), lower (↓), or both (↕) limits of the variability range indicated in Table 1.

In addition to the state vector elements, we report in Table 3 the uncertainties in the single-scattering albedo (SSA) ϖ_0 at the 532-nm wavelength. This important optical parameter is derived from the state vector using the Lorenz–Mie theory. We estimate the retrieval uncertain-

Optics EXPRESS

Table 3. State parameters and propagated uncertainties for four sensitivity study cases

	Case 1 urban	Case 2 larger	Case 3 coarse	Case 4 absorbing
r_{eff}, μm	0.17	0.5	1.6	0.12
$\sigma_{3\beta+2\alpha}$, μm	0.09 (52%)	0.18 (36%)	6.16 (385%)$^{\updownarrow}$	0.01 (6%)
~~$\sigma^{\text{reg}}_{3\beta+2\alpha}$, μm~~	~~0.06 (36%)~~	~~0.08 (17%)~~	~~0.72 (45%)~~	~~0.01 (5%)~~
$\sigma^{165^\circ}_{12\gamma+3\beta+2\alpha}$, μm	0.02 (10%)	0.02 (4%)	0.09 (6%)	0.005 (4%)
v_{eff}	0.16	0.2	0.4	0.2
$\sigma_{3\beta+2\alpha}$	0.24 (152%)$^{\downarrow}$	0.40 (199%)$^{\updownarrow}$	8.7 (2173%)$^{\updownarrow}$	0.06 (32%)
~~$\sigma^{\text{reg}}_{3\beta+2\alpha}$~~	~~0.14 (90%)$^{\downarrow}$~~	~~0.18 (88%)$^{\downarrow}$~~	~~0.20 (50%)$^{\uparrow}$~~	~~0.06 (28%)~~
$\sigma^{165^\circ}_{12\gamma+3\beta+2\alpha}$	0.05 (34%)	0.04 (21%)	0.06 (16%)	0.04 (18%)
m_r	1.47	1.47	1.47	1.67
$\sigma_{3\beta+2\alpha}$	0.18 (12%)$^{\downarrow}$	0.09 (6%)	0.56 (38%)$^{\updownarrow}$	0.22 (13%)
~~$\sigma^{\text{reg}}_{3\beta+2\alpha}$~~	~~0.11 (8%)~~	~~0.05 (3%)~~	~~0.03 (2%)~~	~~0.15 (9%)~~
$\sigma^{165^\circ}_{12\gamma+3\beta+2\alpha}$	0.03 (2%)	0.004 (0.3%)	0.005 (0.3%)	0.13 (8%)
m_i	0.003	0.003	0.003	0.27
$\sigma_{3\beta+2\alpha}$	0.030 (1027%)$^{\downarrow}$	0.012 (406%)$^{\downarrow}$	0.012 (398%)$^{\downarrow}$	0.48 (179%)$^{\updownarrow}$
~~$\sigma^{\text{reg}}_{3\beta+2\alpha}$~~	~~0.021 (689%)$^{\downarrow}$~~	~~0.008 (279%)$^{\downarrow}$~~	~~0.002 (65%)~~	~~0.14 (53%)$^{\uparrow}$~~
$\sigma^{165^\circ}_{12\gamma+3\beta+2\alpha}$	0.005 (152%)$^{\downarrow}$	0.001 (49%)	0.0005 (18%)	0.19 (70%)$^{\uparrow}$
N_c, cm^{-3}	1100	1100	50	1100
$\sigma_{3\beta+2\alpha}$, cm^{-3}	2498 (227%)$^{\downarrow}$	2798 (254%)$^{\downarrow}$	4658 (9316%)$^{\downarrow}$	515 (47%)
~~$\sigma^{\text{reg}}_{3\beta+2\alpha}$, cm^{-3}~~	~~1666 (152%)$^{\downarrow}$~~	~~1260 (115%)$^{\downarrow}$~~	~~119 (237%)$^{\downarrow}$~~	~~410 (37%)~~
$\sigma^{165^\circ}_{12\gamma+3\beta+2\alpha}$, cm^{-3}	551 (50%)	354 (32%)	35 (71%)	310 (28%)
ϖ_0 (at 532 nm)	0.98	0.97	0.91	0.47
$\sigma_{3\beta+2\alpha}$	0.14 (14%)	0.10 (10%)	0.19 (21%)	0.53 (113%)
~~$\sigma^{\text{reg}}_{3\beta+2\alpha}$~~	~~0.10 (10%)~~	~~0.07 (7%)~~	~~0.06 (6%)~~	~~0.16 (35%)~~
$\sigma^{165^\circ}_{12\gamma+3\beta+2\alpha}$	0.03 (3%)	0.01 (1%)	0.01 (1%)	0.26 (56%)

ties in the SSA using the propagated errors in the imaginary part of the refractive index (m_i), which is the main contributor to the SSA variability. Specifically, we first compute the SSA for m_i and $m_i \pm \sigma_{m_i}$ (if $m_i - \sigma_{m_i}$ is negative, the zero value is taken instead). Then we compare the values of $\varpi_0(m_i - \sigma_{m_i}) - \varpi_0(m_i)$ and $\varpi_0(m_i) - \varpi_0(m_i + \sigma_{m_i})$ and take the largest of these differences (in the absolute-value sense) as the estimate of the SSA retrieval accuracy.

Case 1 (Fig. 1) represents a typical fine-mode urban/industrial aerosol which is weakly absorbing ($\varpi_0 = 0.98$). The "$3\beta+2\alpha$" approach performs relatively well in this case, with both r_{eff} and v_{eff} retrieval uncertainties satisfying the (absolute) accuracy thresholds of Table 2. Rodgers'

Optics EXPRESS

Table 4. Number of degrees of freedom for the four sensitivity study cases

DOF	Case 1 urban	Case 2 larger	Case 3 coarse	Case 4 absorbing
# (SV $\gtrsim$ 1)				
$\sigma_{3\beta+2\alpha}$	4	4	3+	4
$\sigma^{165^\circ}_{12\gamma+3\beta+2\alpha}$	5	5	5	4
d_s				
$\sigma_{3\beta+2\alpha}$	4.29	4.18	3.48	3.75
$\sigma^{165^\circ}_{12\gamma+3\beta+2\alpha}$	4.92	4.96	4.90	4.19

regularization artificially reduces the "$3\beta + 2\alpha$" uncertainties by 1/4 to 1/3, yet cannot help reach the accuracy targets for the refractive index, number concentration, and SSA retrievals. "$12\gamma + 3\beta + 2\alpha$" shows a much better performance, with propagated errors being at least five times smaller than those of "$3\beta + 2\alpha$" and fulfilling all the requirements listed in Table 2. Even the relatively poor accuracy (152%) of the m_i retrieval translates into a satisfactory uncertainty in the SSA of only 0.03.

Case 2 (Fig. 2) is similar to Case 1, except with larger particles (and a slightly larger v_{eff}). The "$12\gamma + 3\beta + 2\alpha$" technique shows in this case an even better accuracy than in Case 1, with all retrievals meeting their accuracy targets. In comparison, "$3\beta + 2\alpha$" performs generally worse than in the previous case: none of the retrieval accuracies satisfy the requirements of Table 2 (even with the help of regularization).

The aerosol in Case 3 (Fig. 3) consists of coarse-mode particles such as those found in sea spray. Their concentration is lower (50 vs. 1100 cm^{-3}) and the size distribution is wider (v_{eff} = 0.4) than in the first two cases, while the refractive index is the same. The "$12\gamma + 3\beta + 2\alpha$" approach shows similar or better results (except for N_c) compared to Cases 1 and 2, again with all the retrievals meeting the requisite accuracy thresholds. However, this case appears to be the worst for the "$3\beta + 2\alpha$" configuration. The propagated errors for this method appear to be so large that they make all state variables virtually non-retrievable. The range within one standard deviation from the mean of r_{eff}, v_{eff}, and m_r exceeds both their upper and lower expected variability limits listed in Table 1. We should note that when the errors are several times greater than the corresponding values in the model, the results of the linearized approach of Eq. (23) may not be quantitatively accurate, yet they clearly indicate very poor retrieval quality. This case can serve as a good illustration of the misleading effect of the *a priori* regularization [20] which reduces the uncertainty by a factor up to 40, thereby making really bad retrievals look plausible.

Case 4 (Fig. 4) demonstrates the effect of aerosol absorption on the retrievals. For this purpose we selected the aerosol model representing strongly absorbing brown-carbon spheres which have been observed in an East Asian–Pacific outflow [34]. They have $m_i = 0.27$ corresponding to an SSA of 0.47. We found that such strong absorption allows for accurate retrievals of the number concentration and the size distribution parameters (all meeting the accuracy thresholds for both methods). However, the retrieval accuracy of m_r and the SSA in this case appears to be insufficient for both the "$3\beta + 2\alpha$" and the "$12\gamma + 3\beta + 2\alpha$" approaches (while still being better for the latter one). It is quite instructive to see that in this case the regularized

Optics EXPRESS

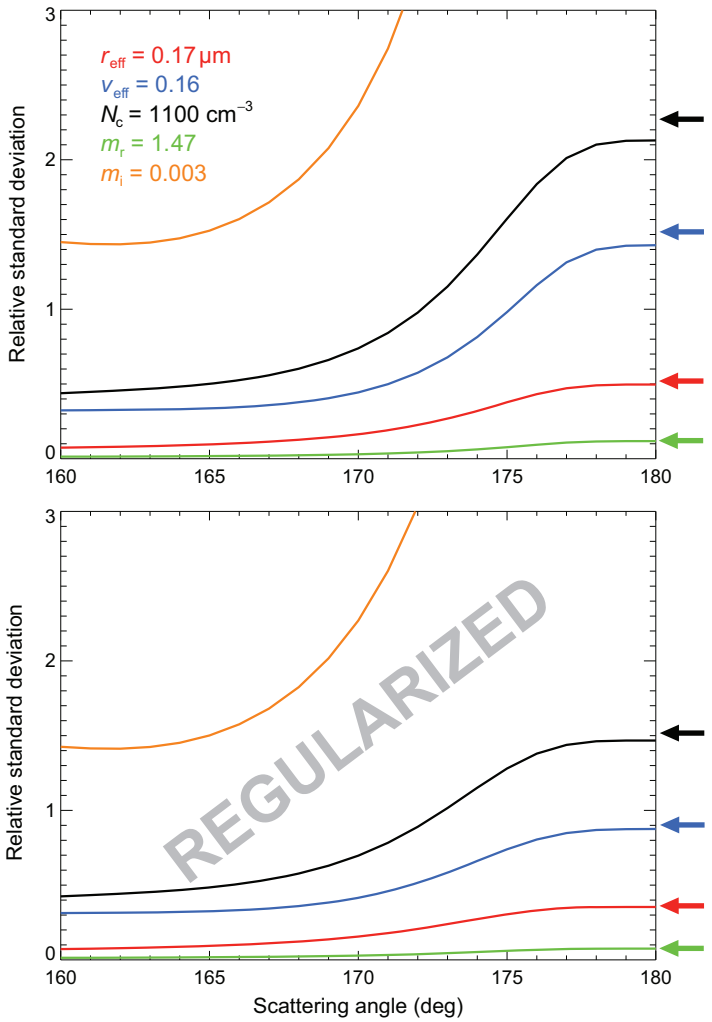

Fig. 1. Ratios of the propagated standard deviations to the actual values of the corresponding state vector elements as functions of the scattering angle Θ for Case 1 (urban fine-mode aerosols). The curves depict the propagated uncertainties of the "$12\gamma + 3\beta + 2\alpha$" method, while those of the "$3\beta + 2\alpha$" approach are shown by the arrows on the right-hand vertical axes. Top: the actual values computed according to Eq. (25); bottom: the values "regularized" according to Eq. (26) (not to be used, shown for comparison only).

"$3\beta + 2\alpha$" retrieval accuracies for the imaginary refractive index and SSA appear to be better than the non-regularized "$12\gamma + 3\beta + 2\alpha$" accuracies. By accepting this result at its face value, one would implicitly conclude that replacing costly actual measurements with "gratis" *a priori* assumptions would be an efficient and inexpensive way to solve the aerosol problem. In reality however this is but another example of misleading results rendered by Eq. (26).

Table 4 and Fig. 5 summarize the information content of the measurements characterized by the number of the degrees of freedom. The first block of rows in Table 4 lists the DOFs determined as the number of SVs of the matrix $\tilde{\mathbf{J}}$ (Eq. (27)) that are greater than unity. This number is the same as the number of eigenvalues of $\tilde{\mathbf{J}}^T\tilde{\mathbf{J}}$ with the same property. The corre-

Optics EXPRESS

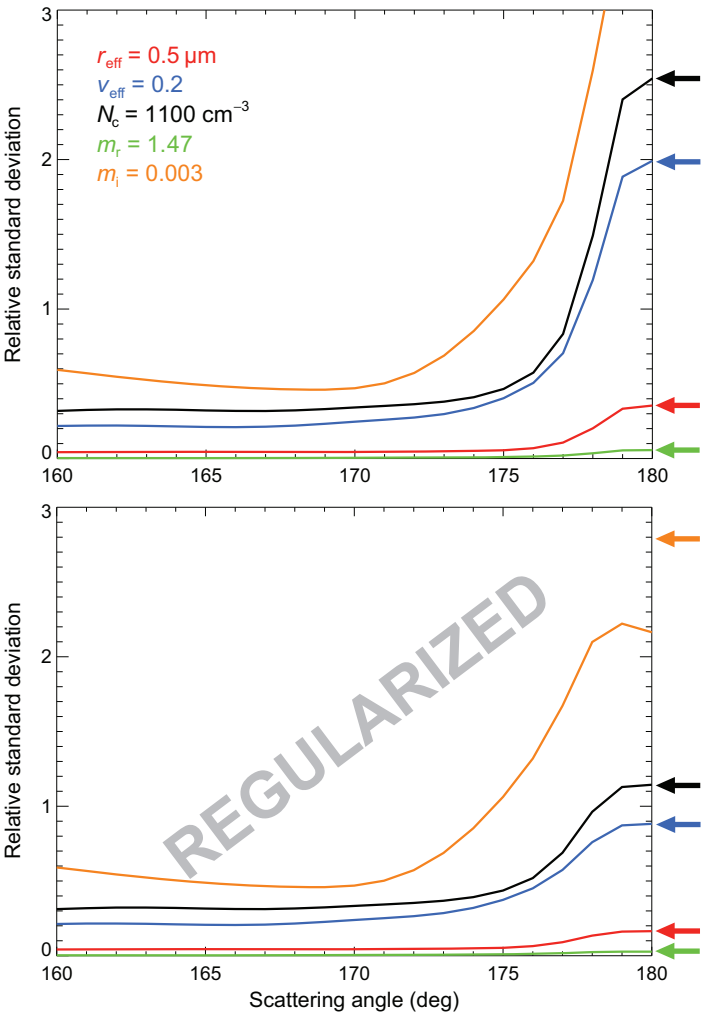

Fig. 2. As in Fig. 1, but for Case 2 (larger aerosols).

sponding data are represented by blue lines and arrows in Fig. 5. We see that in the first three cases the "$12\gamma + 3\beta + 2\alpha$" approach is able to fully characterize the aerosol model showing the maximum possible number of degrees of freedom (five). The DOF is one degree less in Case 4 reflecting poor retrievability of the imaginary part of the aerosol refractive index in this case. The "$3\beta + 2\alpha$" performance is systematically worse, with DOF $\leq$ 4. We assigned this method a DOF of "3+" in Case 3 since it would be three if the strict "greater than unity" criterion is used, however, the second smallest eigenvalue of $\tilde{\mathbf{J}}^T\tilde{\mathbf{J}}$ in this case is 0.94, so it can barely pass the "greater than about unity" test and add the fourth degree of freedom. Note however that in other cases such eigenvalues are substantially larger. The results of the DOF computation in the Bayesian framework according to Eq. (28) are similar (second block of rows in Table 4 and red curves and arrows in Fig. 5). Again, the "$12\gamma + 3\beta + 2\alpha$" methodology performs almost perfectly in Cases 1 – 3 with the corresponding DOFs within 0.1 of the state space dimension (five). The corresponding "$3\beta + 2\alpha$" values are below 4.3, especially in the worst case of coarse particles (Case 3) where d_s = 3.48. These results are in general agreement with those of Burton

Optics EXPRESS

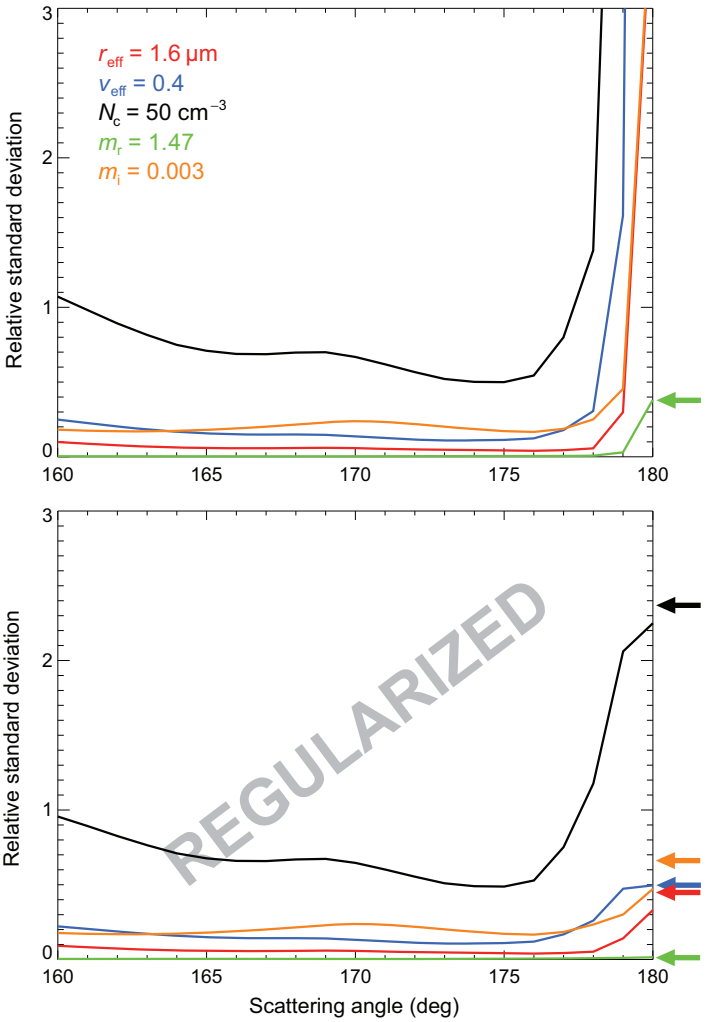

Fig. 3. As in Fig. 1, but for Case 3 (coarse-mode aerosols).

et al. [14], who suggested that the ill-posedness in the "$3\beta + 2\alpha$" approach is primarily caused by cross-talk between the particle radius and number concentration. The improvements in DOFs resulting from the addition of a secondary receiver imply that the supplementary measurements are sufficient to break such cross-talks. In Case 4 both methods show poor ability to constrain m_i of strongly absorbing aerosol. With one effectively non-retrievable parameter, the DOFs for the "$12\gamma + 3\beta + 2\alpha$" and "$3\beta + 2\alpha$" approaches are down to 4.19 and 3.75, respectively.

8. Conclusions

We presented for the first time a quantitative error-propagation study for a bistatic lidar system. Our results demonstrate that the addition of a second receiver (at a scattering angle close to 165°) to a conventional HSRL system leads to a radical improvement of the accuracy of aerosol retrievals. The latter include the effective radius and variance of the aerosol size distribution, complex refractive index, and number concentration. The second receiver provides 12

Optics EXPRESS

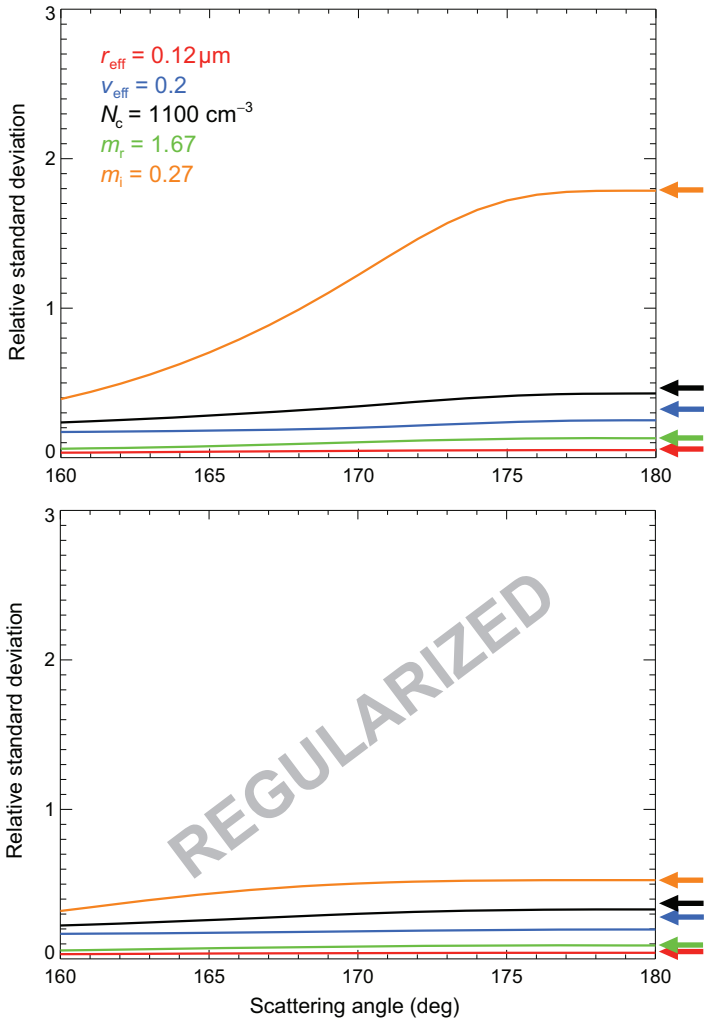

Fig. 4. As in Fig. 1, but for Case 4 (highly absorbing brown-carbon particles).

photopolarimetric measurements in addition to the five measurements of the monostatic lidar. We called this set of measurements "$12\gamma+3\beta+2\alpha$" by analogy with the conventional "$3\beta+2\alpha$" configuration.

In this study the performance of both the "$12\gamma+3\beta+2\alpha$" and the "$3\beta+2\alpha$" techniques was evaluated using the linearized forward model of Eqs. (23) and (25). This approach is similar to that applied to the traditional "$3\beta+2\alpha$" configuration in [14]. Four case-study aerosol models were used in our analysis, three of which represent weakly absorbing aerosols with different sizes, and one simulates highly absorbing brown-carbon particles. The propagated uncertainties summarized in Table 3 show that the "$12\gamma+3\beta+2\alpha$" retrievals are typically much more accurate (with errors smaller by a factor of 5 or more) than their "$3\beta+2\alpha$" counterparts. They always satisfy the threshold accuracy requirements from [14,33] (except for the refractive index and the SSA in Case 4). In contrast, the "$3\beta+2\alpha$" retrieval accuracies failed to satisfy the same requirements for all parameters in all cases, besides r_{eff} and v_{eff} in Cases 1 and 4 and N_c in Case 4. In the cases with weakly absorbing aerosols, the "$3\beta+2\alpha$" approach demonstrated

Optics EXPRESS

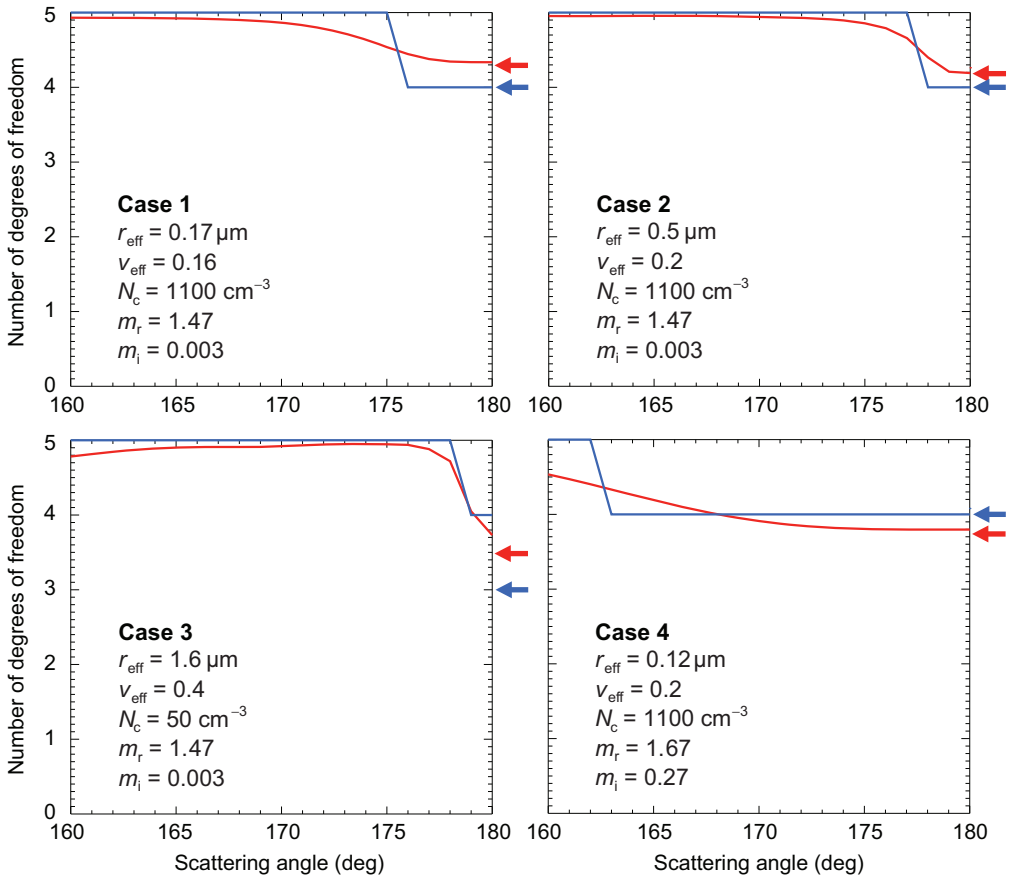

Fig. 5. Degrees of freedom computed for the "$12\gamma + 3\beta + 2\alpha$" approach as functions of the second receiver's scattering angle. The DOFs for the "$3\beta + 2\alpha$" method are indicated by arrows. Blue lines and arrows represent the DOFs determined as the number of eigenvalues of the matrix $\tilde{\mathbf{J}}^T\tilde{\mathbf{J}}$ that are greater than unity ($\tilde{\mathbf{J}}$ is defined by Eq. (27)), while the red curves and arrows represent the DOFs computed according to Eq. (28). The study cases are the same as in Figs. 1–4.

a pronounced accuracy degradation with the increase of the particle size. In particular, for the coarse-mode aerosol in Case 3 virtually none of the aerosol parameters can be considered retrievable using this approach. For the absorbing aerosol in Case 4 both techniques showed good accuracy in size distribution parameters and number concentration, while the estimates of the complex refractive index and the SSA were rather poor. We also demonstrated and discussed how the commonly used *a priori* "regularization" technique of Eq. (26) [20] can artificially reduce the propagated uncertainties and can thus be misleading as to the real retrieval capabilities of a measurement system. The computation of the number of DOFs, an important information content metric, demonstrated that in Cases 1–3 the "$12\gamma + 3\beta + 2\alpha$" technique can fully constrain all aerosol model parameters (the corresponding DOFs being equal to the state vector dimension, i.e., 5), thus resolving cross-talks between state variables present in the "$3\beta + 2\alpha$" approach (where the corresponding DOFs are equal to 4 or less). In Case 4 the poor accuracy of the imaginary refractive index retrieval common to both methods results in DOF = 4.

We conclude that supplementing a monostatic HSRL with an additional receiver would dra-

matically increase the information content of the measurements, allowing for sufficiently accurate and vertically resolved characterization of atmospheric aerosols. Such a bistatic lidar system [16] would far exceed the capabilities of currently available or proposed satellite instruments in monitoring aerosol effects on the Earth's climate.

In this study we do not discuss relevant technical issues (such as, e.g., the configuration and type of the second receiver, the measurement error budget, the degree of separation of aerosol and Rayleigh scattering in HSRL, etc.) and plan to address them elsewhere. Here we only mention the technical feasibility of a fully controlled two-satellite system flying in formation. It has been successfully demonstrated by coordination between the NASA's platforms carrying the Cloud–Aerosol Lidar with Orthogonal Polarization (CALIOP) [35] and the CloudSat radar [36]; and also by the European TanDEM-X (TerraSAR-X add-on for Digital Elevation Measurements) mission based on two radars flying in close formation on twin satellite platforms [37]. Our future plans include similar analyses of more realistic bimodal aerosol populations, as well as more detailed studies involving numerical simulations of the lidar measurements (e.g., using Monte Carlo computations) and the design of inversion algorithms for various bistatic lidar configurations (with an HSR or elastic secondary receiver).

Funding

This research was supported by the NASA Aerosol/Clouds/Ecosystems (ACE) Project managed by Hal Maring and Arlindo da Silva.

Acknowledgments

We appreciate insightful discussions with Brian Cairns, Larry Travis, and Igor Veselovskii as well as three constructive anonymous reviews.